Thulium cross-relaxation in a low phonon energy crystalline host

Joseph Ganem,* Jennifer Crawford, and Paul Schmidt
Department of Physics, Loyola College in Maryland, 4501 N. Charles Street, Baltimore, Maryland 21210

N. W. Jenkins and S. R. Bowman†
Optical Sciences Division, U.S. Naval Research Laboratory, 4555 Overlook Avenue, Washington, DC 20375
(Received 30 May 2002; published 4 December 2002)

We report on the cross-relaxation of Tm^{3+} in a low phonon energy chloride host. The temperature and concentration dependence for Tm^{3+} cross-relaxation in the host YCl_3 was studied between 300 and 500 K, in crystals of YCl_3 with concentrations ranging from 0.7 to 7×10^{20} ions/cm^3. Crystals were grown from melts of anhydrous YCl_3 and $TmCl_3$ powders under Cl_2 atmosphere using a self-seeded vertical Bridgeman technique. Fluorescence spectra and lifetimes resulting from quasi-cw pumping with a 0.5-W, 811-nm diode were collected and analyzed for the spectral region 1100–2000 nm versus temperature for three crystals with varying Tm^{3+} densities. Each of the fluorescence spectra contain three broad features centered at 1200, 1490, and 1800 nm that reflect the populations of the first three excited levels of Tm^{3+}. Rates for multiphonon relaxation and cross-relaxation were determined from the fluorescence lifetime data. An increase in 1200-nm fluorescence as the temperature rises is evidence of an endothermic cross-relaxation process. This suggests a fundamentally new mechanism for optical cooling. A macroscopic rate equation model with its temperature and concentration dependence given by theories for phonon-assisted energy transfer is fit to the spectral data.

DOI: 10.1103/PhysRevB.66.245101 PACS number(s): 78.30.Hv, 42.70.Hj, 63.20.Kr

INTRODUCTION

Trivalent thulium (Tm^{3+}) is a widely used ion in solid-state infrared laser systems. Two features in its electronic energy-level structure are of particular use. One is a strong absorption resonant with low-cost, high-powered, 800-nm laser diodes that makes Tm^{3+} an attractive sensitizing ion for diode pumping laser crystals. Another is an emission from the first excited state near 2 μm, commonly used as a laser transition or to sensitize 2-μm transitions in ions such as holmium.

Commercially available diode pumped 2-μm thulium and thulium-holmium based solid-state laser systems typically use either oxide or fluoride host crystals such as yttrium aluminum garnet (YAG) or $YLiF_4$. Oxide and fluoride hosts are attractive because of their desirable mechanical properties. A crystal such as YAG is hard, nonhygroscopic, and conducts heat well. Because of the many applications (e.g., remote sensing, infrared counter measures) for 2-μm lasers, extensive studies of electron energy dynamics under optical pumping have been conducted on Tm:YAG,[1] Tm:YLF,[2] Tm-Ho YAG,[3,4] Tm:HoYLF,[5] Cr, Tm, Ho:YLF.[6] There have been comparative studies of 2-μm laser materials[7,8] and in the search for additional hosts for Tm^{3+}, other oxides such as Y_2SiO_5, $CaY_4(SiO_4)_3O$, and $SrY_4(SiO_4)_3O$ have also been investigated.[9]

Investigations of rare-earth ions in low phonon energy chloride host crystals have also been reported. The trichlorides, $LaCl_3$ and YCl_3, were used to map the rare-earth energy levels.[10] The fluorescent lifetimes of the infrared levels for most of the rare earths in trichlorides, including for Tm^{3+} in YCl_3, were reported by Gandrud and Moos.[11] While chlorides tend to have poor mechanical properties, their low-energy phonon spectra enable many more metastable states and comparatively long infrared lifetimes. The reduction of multiphonon radiation quenching in chloride crystals has been exploited to demonstrate several different midinfrared laser transitions using rare-earth ions. Lasers based on Pr^{3+} in $LaCl_3$ have been operated at 1.7, 5.2, and 7.2 μm[12,13] with this last transition operating at room temperature. Studies of midinfrared radiation from Er^{3+} to identify possible infrared laser transitions in YCl_3 have been reported.[14,15] The concept of using low phonon hosts to activate infrared laser transitions works in both chloride and sulfide hosts. Low phonon energy sulfides and chlorides have been used for Dy^{3+}-based midinfrared lasers at 2.43 and 4.31 μm in $CaGa_2S_4$ and at 2.43 μm in KPb_2Cl_5.[16–19] The use of KPb_2Cl_5 by Nostrand *et al.*[16–18] for a laser is especially interesting since it is a mechanically stable chloride crystal and demonstrates that practical chloride-based infrared lasers and amplifiers are possible. The midinfrared transitions of Er^{3+} have been studied in the KPb_2Cl_5 host[20,21] and recently a room-temperature 4.6-μm Er^{3+} laser was demonstrated using KPb_2Cl_5.[22] Further studies of the rare-earth ions Dy^{3+} and Nd^{3+} have focused on the KPb_2Cl_5 host.[23–25]

Aside from their ability to radiate in the midinfrared, low phonon energy materials have attracted interest for experiments on optical cooling. Rapid multiphonon quenching in oxide and fluoride hosts generates large amounts of heat and associated problems such as thermal lensing and the need for heat removal. The problem of heat generation in Tm^{3+} lasers is made worse when pumping with 800-nm diodes, since the cross-relaxation process used to transfer energy from the pumped state to the upper laser level is nonresonant and generates phonons to offset the energy excess. Proposals have been made for reducing heat generation in solid-state lasers through the use of anti-Stokes fluorescence.[26–28] Recently optical cooling has been demonstrated in Tm^{3+}-doped[29] and Yb^{3+}-doped[30–32] materials.

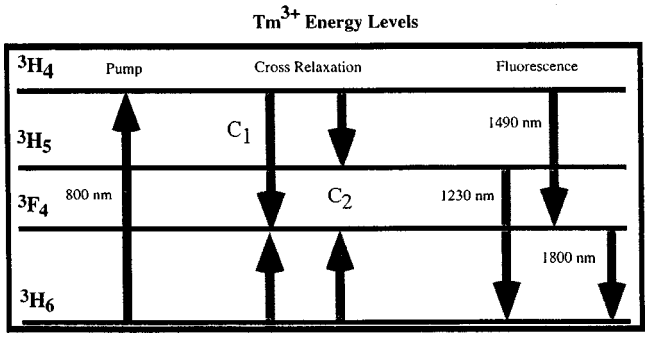

FIG. 1. Lower energy levels of Tm^{3+}. Indicated are the transitions for pumping, cross-relaxation, and emission in Tm^{3+}.

In this paper we report the study of Tm^{3+} cross-relaxation in a low phonon energy chloride host. Our focus is investigating the effects reduced phonon energies have on the concentration and temperature dependence of the cross-relaxation processes that follow diode pumping at 800 nm. We chose YCl_3 as a host material because it has low phonon energies, readily incorporates a wide range of Tm^{3+} densities, and is easy to grow. Figure 1 illustrates the lower energy levels for Tm^{3+}. Low-cost 800-nm diodes are resonant with the $^3H_4$ level that when pumped, cross relaxes to the $^3F_4$ level (the upper laser level in 2-μm lasers) as well as the $^3H_5$ level. The two pathways for cross relaxation, labeled C_1 and C_2, are indicated in Fig. 1. Process C_1, transfers energy to the $^3F_4$, while C_2, populates both the $^3F_4$ and $^3H_5$ levels. While other energy transfer processes are possible, these cross-relaxation processes, because they involve interactions with ground-state ions, have the largest effect on Tm^{3+} excited-state dynamics. Both processes are nonresonant and require sufficient Tm^{3+} density and phonon assistance to be effective. In oxides and fluorides, C_2 is not directly observable because the $^3H_5$ state is completely multiphonon quenched. However, in a chloride host, because the reduced phonon energies enable the $^3H_5$ level to radiate, it is possible to observe C_2, a process that is endothermic because it absorbs phonons.

EXPERIMENT

Four crystals of YCl_3 with concentrations of 0.7, 1.5, 3.0, and 7.0×10^{20} Tm^{3+} ions/cm^3 were grown from melts of anhydrous YCl_3 and $TmCl_3$ powders under Cl_2 atmosphere using a self-seeded vertical Bridgeman technique. Figure 2 shows the overlap of the unpolarized fluorescence spectrum resulting from cw pumping with a 0.5-W, 811-nm diode, with the unpolarized absorption spectrum taken with a Fourier transform infrared (FTIR) spectrometer. Both spectra were obtained at room temperature from the crystal with the greatest Tm^{3+} doping. Fluorescence near 1200 nm from the $^3H_5$ to $^3H_6$ transition appears in the spectrum, a feature not found for Tm^{3+} in oxide hosts.

Unpolarized fluorescence spectra resulting from gated-pumping with 0.35 W of incident power from an 811-nm diode and analyzed with an 0.20-m monochrometer, were obtained at various temperatures between 300 and 500 K for

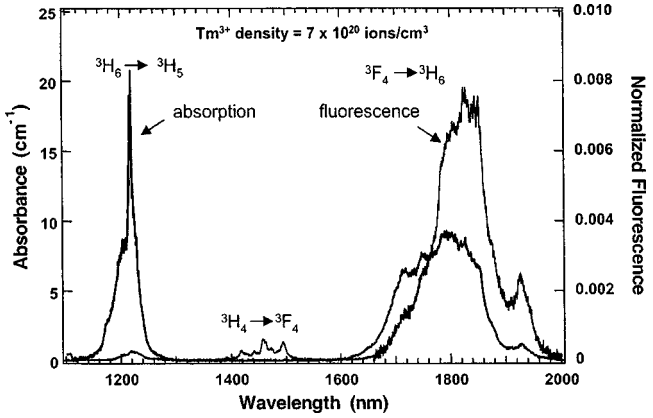

FIG. 2. Overlap of Tm^{3+} absorption and fluorescence. Shown are unpolarized absorption and fluorescence spectra at 300 K for 7×10^{20} ions/cm^3 Tm^{3+} in YCl_3.

the three crystals with the lowest Tm^{3+} densities. The diode was run in quasi-cw mode with 50-ms pulses at a repetition rate of 10 Hz. Pulsing the diode allowed for lock-in detection of the fluorescence between 1100 and 1700 nm with an InGaAs detector. The 50-ms pulse length is five times longer than the longest rise time (10 ms for the 1800-nm fluorescence from the $^3F_4$ state) which means the intensity of features in all the spectra reflect steady-state conditions. Fluorescence detection between 1300 and 2000 nm used a liquid-nitrogen-cooled InSb detector. Complete spectra were obtained by overlapping spectra from the two detectors and matching their common feature centered at 1490 nm.

Each of the fluorescence spectra contain the three broad features seen in Fig. 2 that reflect the populations of the first three excited levels of Tm^{3+} shown in Fig. 1. The most intense fluorescence feature is the broad emission centered near 1800 nm that originates from the long-lived first excited ($^3F_4$) state. Relative to the 1800-nm emission, the intensity of the feature at 1490 nm ($^3H_4-^3F_4$ transition) is controlled primarily by the Tm^{3+} density. Figure 3 compares fluorescence spectra at 300 K for two crystals, one with 0.7×10^{20} Tm^{3+} ions/cm^3 and the other with 3.0

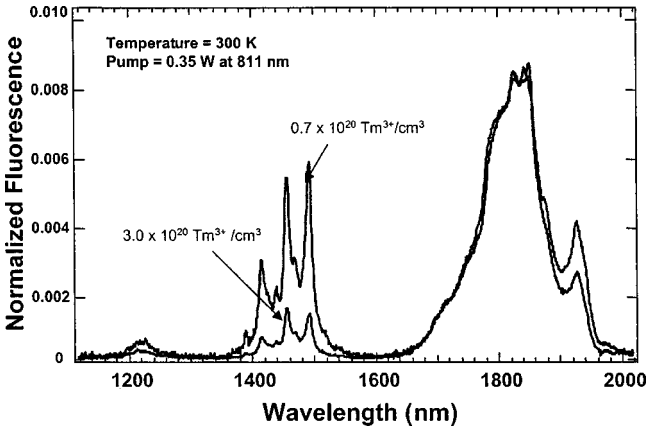

FIG. 3. Effect of concentration of fluorescence. Compared are fluorescence spectra at 300 K for 3×10^{20} and 0.7×10^{20} ions/cm^3 Tm^{3+} in YCl_3.

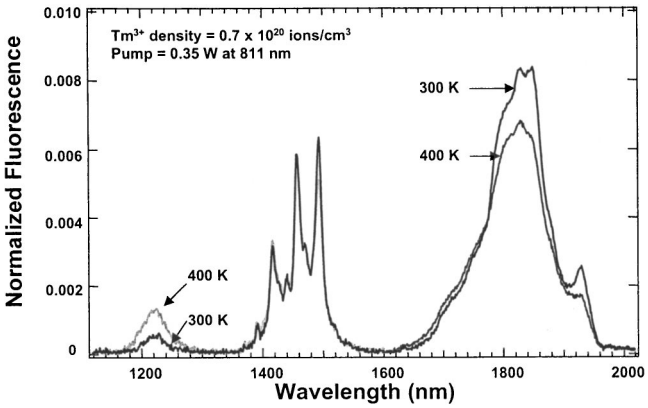

FIG. 4. Effect of temperature on fluorescence. Compared are fluorescence spectra at 300 and 400 K for 0.7 $\times 10^{20}$ ions/cm^3 Tm^{3+} in YCl_3.

$\times 10^{20}$ Tm^{3+} ions/cm^3. The emission intensities, defined as $\int I(\lambda) d\lambda$, are scaled so that for each spectra the 1800-nm feature is normalized to 1. The comparison shows that relative to the 1800-nm emission there is nearly a factor of 5 increase in 1490-nm emission as the Tm^{3+} density is reduced while the relative emission at 1200 nm changes by less than a factor of 2.

Figure 4 depicts the fluorescence spectra of the least concentrated sample at 300 K and at 400 K. As the temperature is increased from 300 to 400 K, there is a small reduction in emission at 1490 nm ($^3H_4$) and 1800 nm ($^3F_4$) but a doubling in 1200-nm emission ($^3H_5$).

The combined effects of varying temperature and Tm^{3+} density are summarized in Figs. 5(a)–(c), that show for three concentrations of Tm^{3+}, the relative intensities of the three emission lines: 1200, 1490, 1800 nm, as a function of temperature. Figure 5 shows that above 400 K, rapid multiphonon quenching associated with high temperatures reduces fluorescence from all three levels. Below 400 K, the intensities (relative to the 1800-nm line) of the 1490 and 1200 nm lines decrease as the Tm^{3+} concentration is increased. However, from 300 to 400 K, for each Tm^{3+} concentration there is a factor of 2 increase in 1200-nm emission as the temperature rises.

Lifetime measurements for each of the excited states were obtained by gating the 800-nm cw pump and recording the transient rise and decay of fluorescence using an InGaAs photodetector at the exit slits of the monochrometer. Fluorescence transients at 1490 nm (from the $^3H_4$ level), 1200 nm (from the $^3H_5$ level) and 1700 nm (from the $^3F_4$ level) were recorded between 300 and 500 K at 50 K temperature intervals for three crystals. Figure 6 shows the room-temperature decay of 1490-nm fluorescence originating from the $^3H_4$ level for the three crystals with Tm^{3+} densities of 0.7, 1.5, and 3×10^{20} ions/cm^3. Decays from the $^3H_4$ level are exponential and concentration quenched since their time constants decrease as Tm^{3+} density increases.

The temperature dependence of the lifetime for $^3H_4$ level is shown in Fig. 7. For the crystal with Tm^{3+} density 0.7 $\times 10^{20}$ ions/cm^{3+}, 1490-nm fluorescence decays are shown for increasing temperatures. All three crystals and all three levels shown a decrease in decay times as the temperature increases.

Table I summarizes the fluorescence lifetimes and their uncertainties for each crystal as a function of temperature. All decays from the $^3H_4$ and $^3F_4$ levels were found to be exponential and their lifetimes are characterized by an exponential time constant obtained from a fit of the intensities to a relation $I=I_0 e^{-t/\tau}$. For the $^3H_5$ level, decays become nonexponential as the temperature increases. Nonexponential decays are marked in Table I with an asterisk and $1/e$ times reported. Uncertainties tend to increase as the Tm^{3+} density is reduced and the temperature is increased, because in both cases the overall fluorescence is reduced. Lifetimes of the $^3H_5$ and $^3F_4$ levels are strongly temperature dependent but show little variation with Tm^{3+} density. For the $^3H_4$ level, lifetimes depend on both temperature and Tm^{3+} density, as shown in Figs. 6 and 7.

THEORY

Chloride hosts are characterized by reduced multiphonon relaxation rates which enables more radiative and energy transfer processes than found in oxide hosts. For the YCl_3 host, Tm^{3+} cross-relaxation is controlled by a distance-dependent electric dipole-dipole interaction between neighboring Tm^{3+} ions, mediated by an electronic coupling to the lattice phonons. Varying the Tm^{3+} density demonstrates the distance dependence of the dipole-dipole interaction. Varying the availability of phonons by controlling the temperature demonstrates the role phonons play in the cross-relaxation as well as the effect of increased multiphonon relaxation rates. Theories for energy transfer, both with and without phonon assistance, are discussed first. The theories are then used to construct a macroscopic rate model that describes the Tm^{3+} dynamics.

Energy transfer

For two ions designated *s* (sensitizer) and a (acceptor) separated by a distance *R*, the rate for electric dipole-dipole resonant transfer of energy is given by Dexter's formula,[33]

$$W_{sa}=(W_s/R^6)(3/4\pi) \times(\hbar c/\pi n)^4 Q_a \int (1/E^4) f_s^{ems}(E) f_a^{\mathrm{abs}}(E) dE, \quad (1)$$

where W_s, the rate in the absence of energy transfer, is the rate at which the sensitizer ions radiate. In this expression *n* is the index of refraction, Q_a is the integrated absorption cross section of the acceptor ion $\int \sigma(E) dE$, and f_s^{ems} and f_a^{abs} are the normalized $[\int f(E) dE = 1]$ emission and absorption spectra with *E* the photon energy equal to hc/λ. Equation (1) can be written in the form

$$W_{sa}=W_s(R_{\mathrm{cr}}/R)^6, \quad (2)$$

where R_{cr} the critical interaction distance, is the distance between sensitizers and acceptors for which the energy-transfer rate W_{sa} is equal to W_s. Therefore effective energy

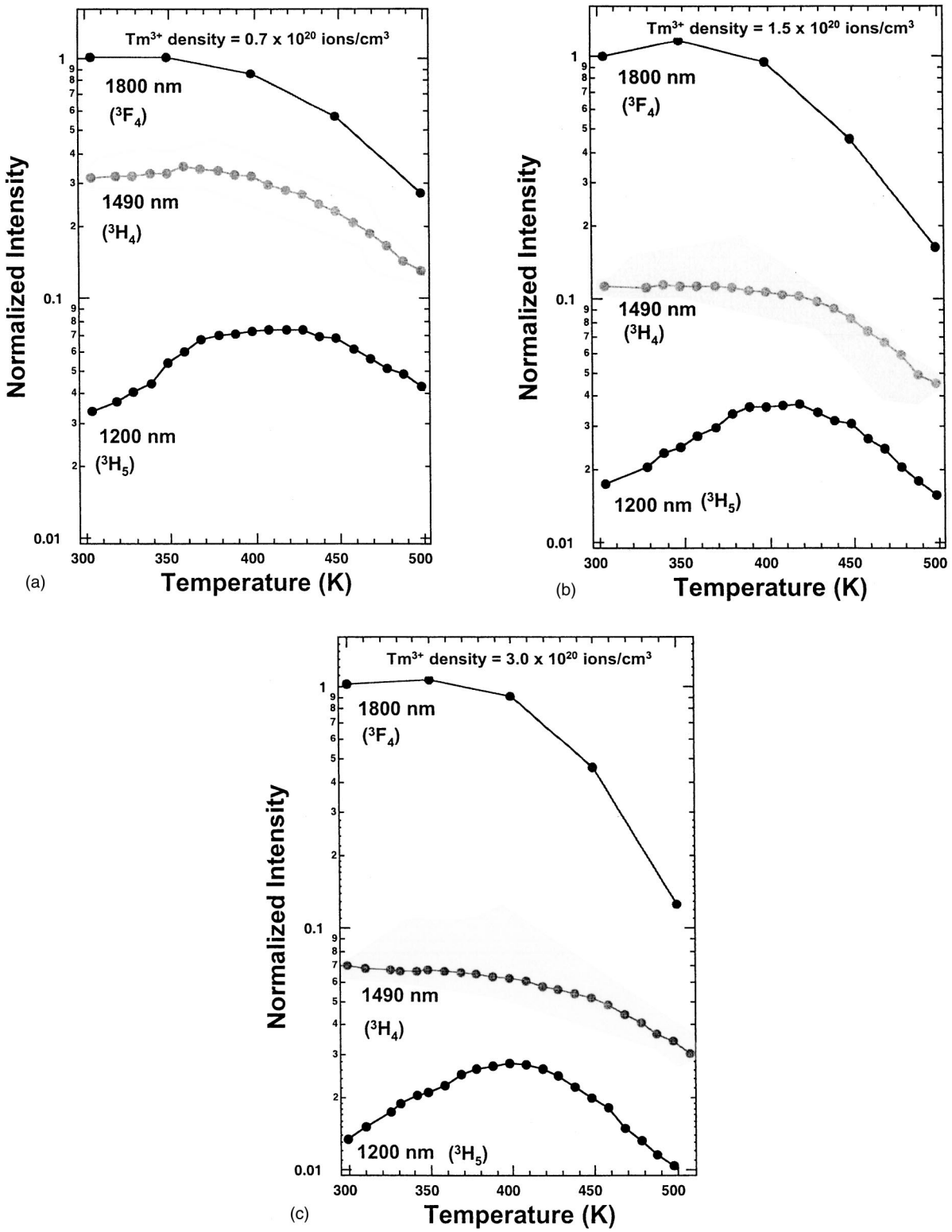

FIG. 5. Summary of fluorescence intensity data. The fluorescence intensity for Tm^{3+} infrared transitions versus temperature for three concentrations: (a) 0.7×10^{20}, (b) 1.5×10^{20}, and (c) 3×10^{20} ions/cm^3 Tm^{3+} in YCl_3. The room-temperature $^3F_4$ population for each sample is normalized to 1.

transfer requires both sufficient ionic density and sufficient overlap of the absorption and emission spectra so that the critical interaction distance is of order of the typical distance between sensitizers and acceptors.

Phonon-assisted energy transfer

In the absence of energetic overlap between donor and acceptor ions, energy transfer is still possible with phonon

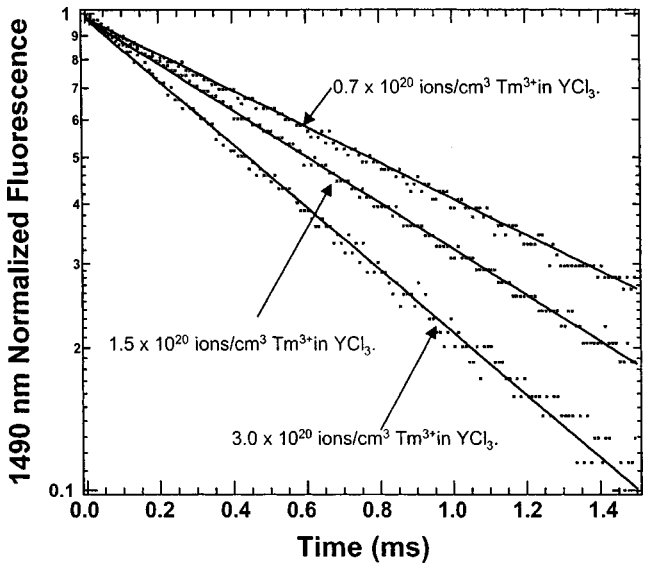

FIG. 6. Concentration quenching of the $^3H_4$ level. Comparison of 1490-nm fluorescence decays from the $^3H_4$ level at 300 K for three concentrations: 0.7×10^{20}, 1.5×10^{20}, and 3×10^{20} ions/cm^3 Tm^{3+} in YCl_3. Solid lines are exponential fits.

mediation. Equation (1) is still applicable but the overlap integral must be modified to include the phonon sidebands. When the energy mismatch becomes of order 10^3 cm^{-1}, multiphonon processes must be considered. The theory of Miyakawa and Dexter[34] predicts that multiphonon-assisted processes obey exponential energy gap laws. For multiphonon relaxation (MPR) the energy gap dependence is

$$W_{\mathrm{MPR}}(\Delta E)=W_{\mathrm{MPR}}(\Delta E=0)e^{[-\alpha(\Delta E)]}, \tag{3}$$

where $W_{\mathrm{MPR}}(0)$ is the rate in the absence of an energy difference. Similarly for multiphonon-assisted energy transfer the dependence is

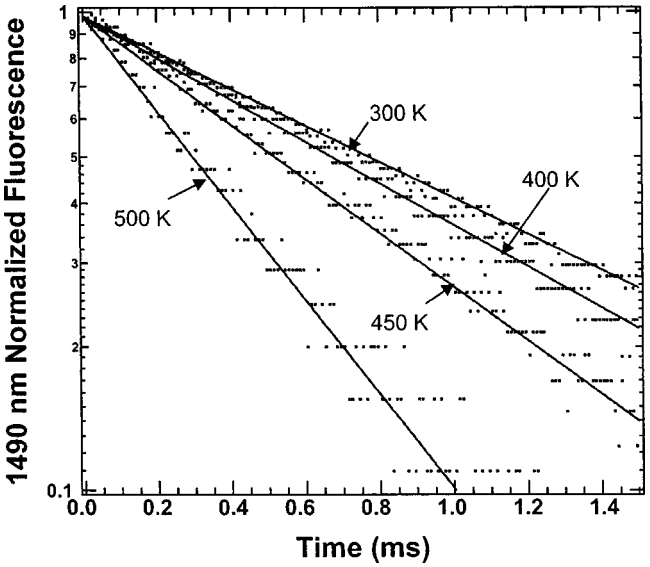

FIG. 7. Multiphonon quenching of the $^3H_4$ level. Comparison of 1490-nm fluorescence decays from the $^3H_4$ level at 300, 400, 450, and 500 K for 0.7×10^{20} ions/cm^3 Tm^{3+} in YCl_3. Solid lines are exponential fits.

$$W_{\mathrm{PAT}}(\Delta E)=W_{\mathrm{PAT}}(\Delta E=0)e^{[(-\beta\Delta E)]}, \tag{4}$$

where

$$\beta=\alpha-\gamma \tag{5}$$

and α and γ are

$$\alpha=(\hbar\omega)^{-1}\{\ln[N_i/g(n+1)]-1\} \tag{6}$$

and

$$\gamma=(\hbar\omega)^{-1}\ln[1+g_s/g_a]. \tag{7}$$

In these expressions $\hbar\omega$ is the maximum energy of the lattice phonons, $N_i=\Delta E/\hbar\omega$ is the number of phonons involved in the process, and n the phonon occupation number. The g's are the electron-phonon coupling parameters, g_s is for the sensitizer ions, and g_a the acceptor ions. The exponential energy-gap laws, Eqs. (1) and (2), are approximations since the parameter α also depends on the energy gap as well as the temperature. However, because α depends primarily on $\hbar\omega$, with all other dependencies appearing in the logarithm [Eq. (4)], α is usually treated as a constant for a given lattice. Since α increases as phonon energies ($\hbar\omega$) are decreased, low phonon energy lattices are associated with reduced phonon-assisted relaxation rates. Auzel[35] has shown that experimentally the maximum lattice phonon energy ($\hbar\omega$) is in fact the most important factor in determining α, and worked out a simplified experimental relationship inferred from room-temperature data for the dependence of α on $\hbar\omega$:

$$\alpha(\hbar\omega)=5\times10^{-2}\exp(-6.5\times10^{-3}\hbar\omega), \tag{8}$$

where α is in cm. This relationship is valid in the range of phonon energies $175<\hbar\omega<500$ cm^{-1}. For YCl_3, with $\hbar\omega=260$ cm^{-1}, Eq. (6) predicts that $\alpha=9\times10^{-3}$ cm. If we assume that $g_a=g_b$, then substituting Eq. (5), into Eq. (3) and using $\alpha=9\times10^{-3}$ cm, the prediction for YCl_3 is that $\beta=6.5\times10^{-3}$ cm. Although these values for α and β are inferred from room-temperature data, since their temperature dependence also appears in the argument of the logarithm in Eq. (4), it is assumed that their temperature dependence is weak.

At low temperatures, relaxation processes that emit phonons can proceed through spontaneous emission. As the temperature is raised, phonon occupation increases, which allows for stimulated emission of phonons. Therefore the temperature-dependent rates for phonon-emitting processes are

$$W_e(T)=W_e(T=0)(1+n)^{N_e}, \tag{9}$$

where N_e is the number of phonons ($\Delta E/\hbar\omega$) emitted to fill the energy gap for the phonon-assisted process and n the phonon occupation number.[36]

Phonon-absorbing processes require occupation of the phonon states, their rates have a stronger temperature dependence given by

$$W_a(T)=W_a(T=0)(n)^{N_a}, \tag{10}$$

TABLE I. Measured fluorescence lifetimes for three emission wavelengths as a function of temperature for three samples: (a) 0.7×10^{20}, (b) 1.5×10^{20}, and (c) 3×10^{20} ion/cm^3 Tm^{3+} in YCl_3. An asterisk (*) indicates a nonexponential decay with a $1/e$ time reported.

(a) Tm^{3+} density$=0.7\times10^{20}$ ions/cm^3			
Temperature (K)	$^3H_5$ τ (ms) 1200 nm	$^3H_4$ τ (ms) 1490 nm	$^3F_4$ τ (ms) 1700 nm
300	9.1±0.5	1.2±0.1	8.0±2.2
350	*7.5±1.0	1.0±0.1	8.0±1.0
400	*4.4±0.2	0.74±0.01	5.1±1.5
450	*1.8±0.1	0.59±0.02	3.5±1.0
500	*1.15±0.1	0.37±0.01	1.4±0.4
(b) Tm^{3+} density$=1.5\times10^{20}$ ions/cm^3			
Temperature (K)	$^3H_5$ τ (ms) 1200 nm	$^3H_4$ τ (ms) 1490 nm	$^3F_4$ τ (ms) 1700 nm
300	8.6±0.2	0.9±0.01	9.9±0.03
350	7.5±0.3	0.85±0.02	8.0±0.05
400	4.2±0.1	0.72±0.01	5.9±0.02
450	*1.5±0.1	0.55±0.03	2.5±0.02
500	*0.55±0.1	0.29±0.03	0.68±0.1
(c) Tm^{3+} density$=3\times10^{20}$ ions/cm^3			
Temperature (K)	$^3H_5$ τ (ms) 1200 nm	$^3H_4$ τ (ms) 1490 nm	$^3F_4$ τ (ms) 1700 nm
300	9.5±0.5	0.72±0.03	9.1±.02
350	7.4±0.2	0.55±0.02	8.1±0.2
400	4.5±0.1	0.52±0.02	5.6±0.3
450	*1.7±0.1	*0.28±0.2	2.4±0.2
500	*0.35±0.2	*0.2±0.1	0.9±0.1

where N_a is the number of phonons absorbed.[35] The temperature dependence of the phonon-assisted transfer rates Eqs. (6), (9), and (10) results from a Bose-Einstein distribution of the phonon occupation number:

$$n=(e^{[\hbar\omega/kT]}-1)^{-1}, \tag{11}$$

where $\hbar\omega$ is the highest allowed phonon energy (260 cm^{-1} in YCl_3). The maximum allowed phonon energy is the most important parameter in controlling both the temperature and energy-gap dependence of all phonon-assisted relaxation processes.

Equations (9) and (10) are for the idealized case of phonon-assisted energy transfer from a single level. In general energy transfer originates from a Stark multiplet with a width of several hundred cm^{-1}. Since the Stark levels thermalize on a time scale that is short compared to energy-transfer rates, the observed rates are given by a weighted average,

$$W(1/Z)\sum_i q_i W_i \exp(-\Delta_i/kT), \tag{12}$$

where Δ_i is the energy difference of the ith level from the bottom Stark level, q_i is the degeneracy of the ith level, W_i is the multiphonon relaxation rate from the ith level given by either Eqs. (9) or (10), and Z is the partition function associated with the Stark multiplet, $Z=\Sigma_i \exp(-\Delta_i/kT)$.[36]

DISCUSSION

Our approach to understanding the emission and lifetime data within the theoretical framework for energy transfer, is to identify all the relevant radiative and nonradiative processes and describe their effects on excited-state populations with coupled time-dependent rate equations. Lifetime data for all three excited states as a function of temperature and density were analyzed to determine the rate constants for the model. Nonradiative processes are assigned the temperature dependence of either Eq. (9) or Eq. (10) depending on whether the process is phonon absorbing or phonon emitting.

While theories of energy transfer based on migration-assisted excitation[37] or the Foster-Dexter mechanism[33,38] are available to predict the time dependence of fluorescence decays, these theories are not adequate for describing multiple coupled levels. Our approach is to use a macroscopic rate model with coupled time-dependent equations to describe the excited-state dynamics. The macroscopic rate model developed will account for the change of the $^3H_5$ decays from

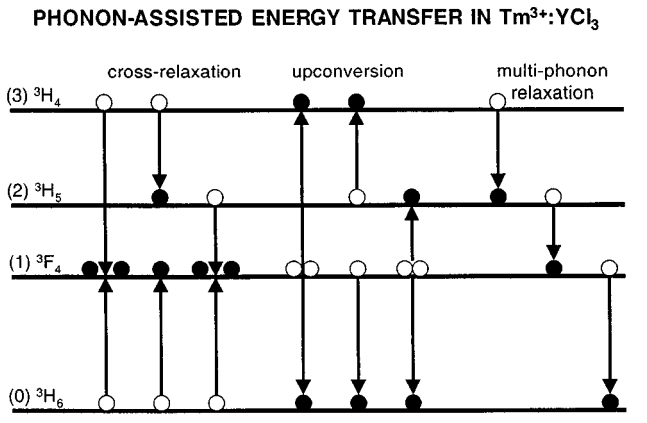

Rate	C_1	C_2	C_3	U_1	U_2	U_3	M_{32}	M_{21}	M_{10}
ΔE (cm^{-1})	698	-641	-2177	-698	641	2177	4000	2319	5149
# phonons = $\Delta E/\hbar\omega$	3	-3	-9	-3	3	9	15	9	20

FIG. 8. Phonon-assisted nonradiative energy-transfer processes and associated energy gaps for Tm^{3+} in YCl_3.

exponential to nonexponential as the temperature is increased. The change in decay behavior arises because competing energy-transfer terms in the rate equations have different temperature dependencies.

The analysis procedure consists of identifying the most probable energy-transfer processes, which include spontaneous emission, cross-relaxation, upconversion, and multiphonon relaxation, all shown schematically in Fig. 8. A set of coupled macroscopic rate equations for the time-dependent level populations [Eqs. (13a)–(13d)] are expressed, each with unknown rate constants. Each rate constant is determined individually, with an estimate of its value made using the available fluorescence lifetime and intensity data. For the constants associated with phonon-assisted energy transfer, the values are compared to the existing models for either their temperature or density dependence. Spontaneous emission rates are assumed to be temperature and density independent. Once most of the rate constants are known, results from the entire rate model are fit to the transient emission data to determine the remaining unknown rates. Finally the rate model results are compared to the data for emission intensity versus temperature for all three excited states.

Energy-transfer processes

The fluorescence feature centered at 1490 nm (Figs. 2 and 3) results from the $^3H_4$ to $^3F_4$ transition. There is no overlap of the 1490-nm feature with either of the two absorptions, $^3H_6$–$^3F_4$ and $^3H_6$–$^3H_5$, which illustrates the nonresonant nature of the cross-relaxation processes shown in Fig. 1. The lack of overlap shows that cross-relaxation to either the $^3F_4$ or $^3H_5$ results in an energy mismatch that necessitates the assistance of phonons. Additional phonon-assisted energy-transfer processes connecting the four lowest levels of Tm^{3+} are present, these include upconversion and multiphonon relaxation. Figure 8 is a schematic diagram of the four lowest energy levels for Tm^{3+}:YCl_3 with the primary energy-transfer processes indicated. All processes shown in Fig. 8 require either phonon creation or annihilation to bridge the energy gap (ΔE). For each process the energy gap is computed using the low-temperature energy-level data of Dieke[10] for Tm^{3+}:YCl_3. Since each of the four levels in Fig. 8 is a multiplet of Stark levels, the energy gaps listed are the minimum possible. For example, the gap for process C_1 is the energy difference between the transition up from the lowest Stark level of the $^3H_6$ to the highest level of the $^3F_4$ and the transition down from the lowest Stark level of the $^3H_4$ to the highest level of the $^3F_4$. Processes with positive energy gaps indicate energy excess (exothermic), and processes with negative gaps indicate energy must be absorbed to complete the transfer (endothermic). The number of phonons each process either emits (positive number) or absorbs (negative number) is obtained by dividing the energy gap by the maximum lattice phonon energy for YCl_3, $\hbar\omega = 260\ cm^{-1}$. C_1 is the rate for the well-known "two for one" process shown in Fig. 8 where an ion in the $^3H_4$ level cross-relaxes with a ground state $^3H_6$ ion to produce two $^3F_4$ ions. Processes C_3, U_1, and U_3 are documented in Tm^{3+}:YAG by Shaw *et al.*[1] Cross-relaxation to the $^3H_5$ (C_2) and up-conversion from the $^3H_5$ (U_2) has not been observed for Tm^{3+} in fluoride and oxide hosts because of strong multiphonon quenching of the $^3H_5$. Use of a chloride host for this work allows the study of energy transfer into and out of the $^3H_5$ state.

Macroscopic rate equations

The relative populations of the four lowest excited levels are modeled with the coupled time-dependent rate equations:

$$dn_3/dt = P(t)n_0 - A_{30}n_3 - A_{31}n_3 - A_{32}n_3 - C_1n_0n_3 - C_2n_0n_3 + U_1n_1^2 + U_2n_1n_2 - M_{32}n_3, \quad (13a)$$

$$dn_2/dt = -A_{20}n_2 - A_{21}n_2 + A_{32}n_3 + C_2n_0n_3 - U_2n_1n_2 + U_3n_1^2 + M_{32}n_3 - M_{21}n_2, \quad (13b)$$

$$dn_1/dt = -A_{10}n_1 + A_{31}n_3 + A_{21}n_2 + 2C_1n_0n_3 + C_2n_0n_3 - 2U_1n_1^2 - U_2n_1n_2 - 2U_3n_1^2 + M_{21}n_2 - M_{10}n_1, \quad (13c)$$

$$dn_0/dt = -P(t)n_0 + A_1n_{10} + A_{20}n_2 + A_{30}n_3 - C_1n_0n_3 - C_2n_0n_3 + U_1n_1^2 + U_2n_1n_2 + U_3n_1^2 + M_{10}n_1, \quad (13d)$$

where n_i is the time-dependent population of the ith level. In these equations n_0 is the ground ($^3H_6$) level, n_1 the $^3F_4$, n_2 the $^3H_5$, and n_3 the $^3H_4$. The A_{ij}'s are the spontaneous emission rates from the ith level to the jth level determined by multiplying the branching ratio β_{ij} by the total radiative relaxation rate A_i. The $P(t)$ term represents the duration of the quasi-cw pump pulse. The M_{ij}'s are the multiphonon relaxation rates to the nearest lower level. With the exception of C_3 the rate equations include nonlinear terms that represent the cross-relaxation and up-conversion processes dia-

grammed in Fig. 8. According to Eqs. (9) and (10), phonon-absorbing processes are less probable than phonon emitting processes, and therefore process C_3 that requires the absorption of nine phonons will be negligible compared to the other rates.

Determination of rate constants

The intensities of features in the infrared fluorescence spectra summarized in Fig. 5 show two distinct temperature regimes. Above 400 K multiphonon relaxation is the dominant process. Increasing the temperature from 400 to 500 K results in rapid fluorescence quenching of all levels as the multiphonon rates become much greater than the rates for radiative processes. Below 400 K the multiphonon rates are small compared to the radiative rates. The distribution of energy among the excited states depends on energy transfer processes that for most of the Tm^{3+} densities studied have rates that are of the same order as the radiative rates. Therefore, in estimating parameters for the macroscopic rate model, the high-temperature lifetime data are used to determine multiphonon relaxation rates, and the room-temperature data determine the cross-relaxation, up-conversion, and radiative rates.

Cross-relaxation rates

For a dipole-dipole interaction, the phenomenological rate constants (C_i) for cross-relaxation are given by

$$C_i N = c_{mi}/R^6, \tag{14}$$

where i refers to either process 1 or 2, R is the distance between interacting ions, N is the density of ions in the lattice, and c_{mi} is the microparameter for excitation migration associated with the ith process.[39] For either of cross-relaxation processes C_1 or C_2 to occur, excited-state $^3H_4$ ions must interact with ground-state $^3H_6$ ions. Since incident pump powers (0.35 W) are low, most ions remain in the ground state. Under these conditions the typical distance R between an excited-state ion and a ground-state ion is about equal to the average distance between randomly distributed ions in the lattice, given by

$$R = (1/N)^{1/3}. \tag{15}$$

Substitution of Eq. (15) into Eq. (14) results in

$$C_i = c_{mi} N. \tag{16}$$

For a given electric dipole-dipole interaction the phenomenological rate constants for cross-relaxation are proportional to the microparameter and should increase linearly with ionic density, while the multiphonon and radiative rate constants are density independent. (It will be argued in the next section that up-conversion into the $^3H_4$ is negligible.)

To estimate the rate constants for cross-relaxation we fit the room-temperature inverse lifetimes W_3 for the $^3H_4$ level (Table I) to the relation

$$W_3 = A_3 + c_m N, \tag{17}$$

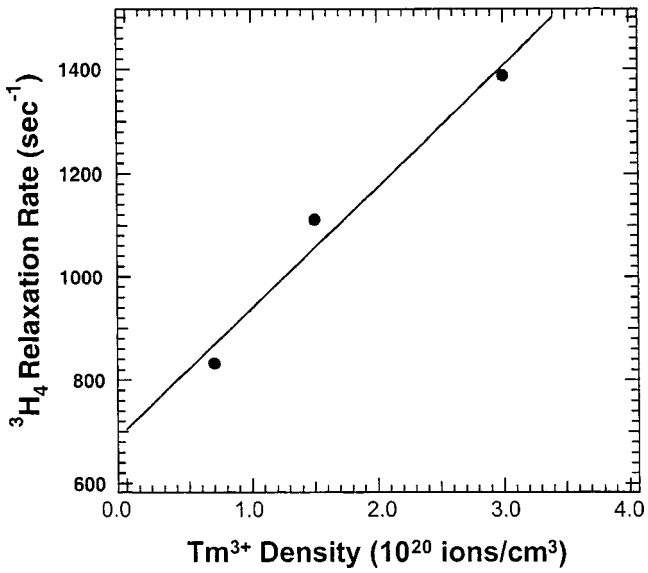

FIG. 9. Cross-relaxation rate of the $^3H_4$ level versus Tm^{3+} density (markers) compared to a linear fit (solid line).

where c_m is the sum of the microparameters for the two cross-relaxation processes, $c_m = c_{m1} + c_{m2}$. Equation (17) assumes that at room temperature M_{32} is negligible. The data points and fit that results in $c_m = 2.3 \times 10^{-18}$ cm^3 sec^{-1} and $A_3 = 700$ sec^{-1} are shown in Fig. 9. Extrapolation to the critical density where the total cross-relaxation rate equals 700 sec^{-1} gives $N_{cr} = 3 \times 10^{20}$ ions/cm^3, which corresponds to an average critical radius at room temperature of $R_{cr} = 15$ Å.

The temperature dependence of the cross-relaxation processes must arise from a temperature-dependent microparameter since the Tm^{3+} density is fixed. Figure 8 shows that C_1 emits three phonons $N_e = \Delta E/\hbar\omega = 3$ and has a temperature dependence given by Eq. (9). C_2 absorbs three phonons $N_a = \Delta E/\hbar\omega = 3$ and has a temperature dependence given by Eq. (10). Combining Eqs. (9) and (10) results in

$$c_m(T) = c_{m1}(T=0)(1+n)^3 + c_{m2}(T=0)n^3. \tag{18}$$

Our rate modeling showed that the zero-temperature microparameters are approximately the same—$c_{m1}(T=0) \approx c_{m2}(T=0) = c_m(T=0)$. Substituting the room-temperature phonon occupation number $n = 0.4$ with the room-temperature result for c_m into Eq. (18) results in $c_m(T=0) = 8.4 \times 10^{-19}$ cm^3 sec^{-1}.

Up-conversion rates

All up-conversion processes shown in Fig. 8 involve excited-state ions. Since the density of excited-state ions is much less than the density of ions in the lattice, the average distance between ions undergoing up-conversion is much greater than for cross-relaxation. Up-conversion out of the $^3F_4$ (processes U_1 and U_3) is favored over up-conversion out of the $^3H_5$ (process U_2), because both the sensitizer and acceptor ions are in the same $^3F_4$ state. As a result the strong overlap between their emission and absorption spectra increases their critical interaction distance [Eq. (1)]. For the

two up-conversion possibilities from the $^3F_4$, the exothermic (U_3) should be much greater than the endothermic (U_1). Therefore only U_3, up-conversion into the $^3H_5$ is considered. Because the $^3H_5$ lifetimes are nonexponential and strongly affected by multiphonon and cross-relaxation, it is not possible to estimate the up-conversion rates from their inverse lifetimes. The up-conversion rates $U_3(N,T)$ were treated as free parameters in the rate equation model and fits made to the transient rise and decay of 1200-nm fluorescence. Fitting the rate equation model to the transients showed the up-conversion rate U_3 to be negligible for all concentrations and temperatures studied. At the low excitation pump powers used in the experiment, the density of excited-state $^3F_4$ ions was never sufficient for significant interactions resulting in up-conversion. The density independence of the $^3F_4$ lifetime (see Table I) is consistent with U_3 being small compared to the other processes and allows us to estimate an upper bound for the U_3 rate constant of $<3\times10^{-20}$ cm^3 sec^{-1}.

Multiphonon relaxation rates

Comparison of low-temperature (4.2-K) lifetime measurements for the $^3F_4$ and $^3H_4$ with room-temperature measurements, indicates that at room temperature multiphonon relaxation rates for these levels are negligible. Gandrud and Moos[11] reported excited-state lifetime measurements at 4.2 K of 8.95 ± 0.55 ms for the $^3F_4$, and 0.547 ± 0.0533 ms for the $^3H_4$. At 300 K they report lifetimes for the $^3F_4$ and $^3H_4$ states, of 8.25 ± 0.67 and 0.588 ± 0.037 ms, respectively, results that are essentially the same as those for 4.2 K (within the margin of error). Their room-temperature result for the $^3F_4$ is in agreement with the room-temperature results reported in Table I. For the $^3H_4$ level, comparison of Gandrud and Moos result with the Table I data indicates that their sample with 1.4×10^{20} Tm^{3+}/cm^3 is concentration quenched due to cross-relaxation. Equation (17) predicts a weak temperature dependence to the cross-relaxation between 4 and 300 K that is not seen in their data. According to Eq. (17), a Tm^{3+} density with a 1-ms lifetime at 4.2 K should shorten to 0.7 ms at 300 K.

To estimate the multiphonon rates for the $^3F_4$ level, we used the high-temperature ($\geq$350 K) fluorescence lifetime data in Table I, for the sample with the lowest Tm^{3+} density (0.7×10^{20} cm^3) in order to minimize the effects of energy transfer. It is assumed that the inverse lifetime at 4.2 K (110 sec^{-1}) is the temperature-independent radiative rate A_{10}. The multiphonon rate M_{10} for the $^3F_4$ is

$$M_{10}=W_1-A_{10}, \tag{19}$$

where W_1 is the total relaxation rate for the $^3F_4$ level which is taken to be the inverse lifetime in Table I.

Figure 10 is a plot of the multiphonon rates for the $^3F_4$ level at temperatures greater than 300 K [obtained from Eq. (19)] compared with a fit to the theoretical temperature dependence for an expected 20-phonon process [Eq. (9) with $\Delta E=5149$ cm^{-1}]. The multiphonon rates fit the temperature dependence for a 20-phonon process. For M_{10} as a function of temperature the result is

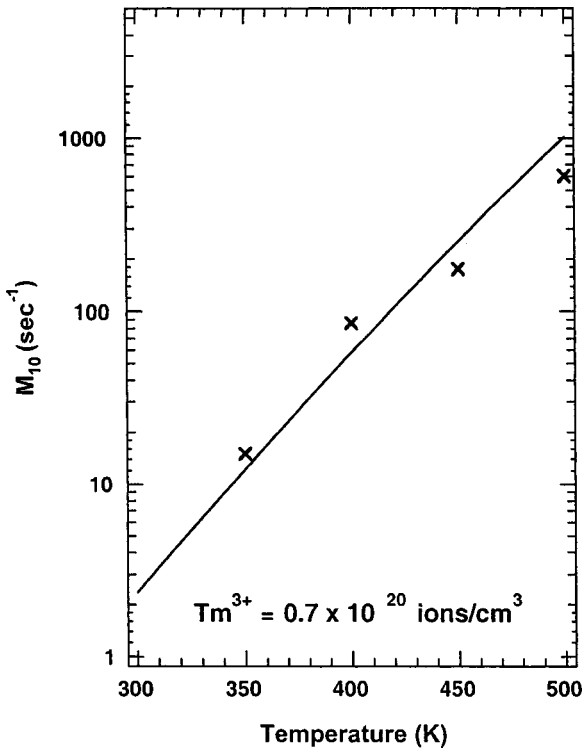

FIG. 10. Multiphonon relaxation rate of the $^3F_4$ level versus temperature (markers) compared to a fit for a 20-phonon process (solid line).

$$M_{10}=0.0025(1+n)^{20}\ \text{sec}^{-1}. \tag{20}$$

For the $^3H_4$ level we also use the data for the sample with the lowest Tm^{3+} density, however, even this sample exhibits cross-relaxation. To determine the multiphonon rates we use

$$M_{32}=W_3-A_3-c_m(T)N, \tag{21}$$

where $c_m(T)$ is given by Eq. (18) and W_3 is the total relaxation rate for the $^3H_4$ level (the inverse lifetimes in Table I). Figure 11 shows the values for M_{32} obtained from Eq. (21) compared to a fit for a temperature dependence associated with a 15-phonon process [Eq. (9) with $\Delta E=4000$ cm^{-1}]. The temperature dependence of M_{32} is

$$M_{32}=0.15(1+n)^{15}\ \text{sec}^{-1}. \tag{22}$$

Equations (20) and (22) predict the multiphonon rates at 300 K to be 15 sec^{-1} for the $^3H_4$ and 21 sec^{-1} for the $^3F_4$, results consistent with our assumption that multiphonon rates for these levels have negligible effects on room-temperature lifetimes. The equations also predict that at 400 K multiphonon rates will overtake energy-transfer rates as the dominant relaxation process. This prediction is consistent with Fig. 5 that shows the onset of fluorescence quenching of all levels at 400 K.

For the $^3H_5$ level, a similar analysis to determine multiphonon relaxation rates breaks down because the fluorescence decay times and rise times are nonexponential (see Table I). The multiphonon rates for the $^3H_5$ were kept as free parameters in the rate model.

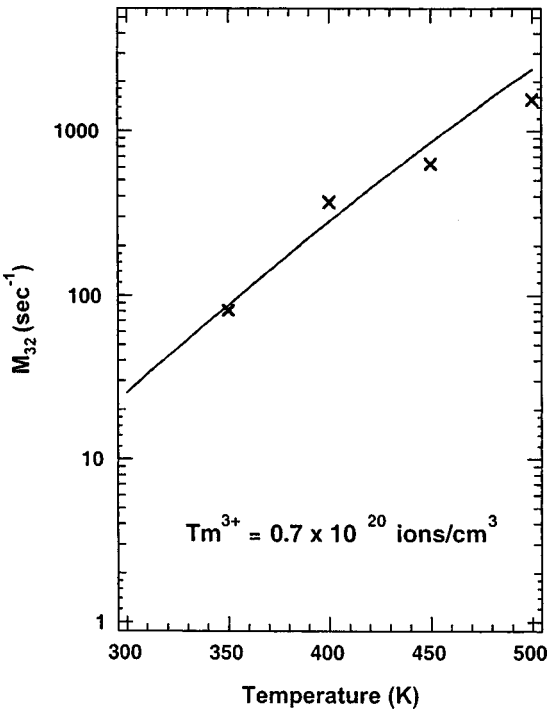

FIG. 11. Multiphonon relaxation rate of the $^3H_4$ level versus temperature (markers) compared to a fit for a 15-phonon process (solid line).

Radiative rates

The fluorescence intensity I is related to the spontaneous emission rate A for ions radiating at frequency ν by

$$I = NAh\nu, \tag{23}$$

where N is the population of ions in the energy level. Therefore the population of the ith energy level N_i is related to the fluorescence intensity of a single transition from that level by

$$N_i = (1/hc\beta_{ij}A_i)\int \lambda_{ij} I(\lambda_{ij})d\lambda, \tag{24}$$

where β_{ij} is the branching ratio for the transition that results in fluorescence of wavelength λ_{ij} and the limits of the integration cover the spectral region associated with the transition from level i to level j. Since the rate equations, Eqs. (13a)–(13d), model relative populations, not emission intensities, knowledge of the spontaneous emission rates can be used in Eq. (24) to infer relative populations from the spectral data on relative emission intensities (Fig. 5).

For the $^3F_4$ level, the room-temperature inverse lifetime W_1, represents the spontaneous emission rate $A_{10} = \frac{1}{9}$ ms $= 110$ sec^{-1}, because the $^3F_4$ lifetime is not affected by increasing the temperature from 4.2 to 300 K[11] or increasing the Tm^{3+} density from 0.7 to 3.0×10^{20} ions/cm^3 (see Table I).

For the $^3H_4$ level the zero-density relaxation rate of 700 sec^{-1} inferred from Fig. 9 equals the total spontaneous emission rate for this level, A_3, because for the $^3H_4$, the room-temperature multiphonon rate is negligible. What is not known for the $^3H_4$ level are the branching ratios, β_{32}, β_{31}, and β_{30}. A search for 2400-nm fluorescence, that would correspond to the $^3H_4$–$^3H_5$ transition, found none. We conclude that branching to the $^3H_5$ can be neglected ($\beta_{32} = 0$). Branching to the $^3F_4$ is clearly present because 1490-nm emission from the transition to the $^3F_4$ is used to monitor the $^3H_4$ population. The branching ratio β_{31} is used as a parameter in the rate model and its value determined by fitting the observed intensity of the 1490-nm emission relative to the other emission lines.

For the $^3H_5$ level, it is expected that from the exponential energy-gap law, Eq. (3), that multiphonon relaxation at room temperature for a nine-phonon process ($\Delta E = 2139$ cm^{-1}) is significant. Gandrud and Moos report a lifetime for the $^3H_5$ of 8.0 ± 1.0 ms at 4.2 K, which shortens to 5.51 ± 0.72 ms, at 300 K, a significant reduction that indicates effective multiphonon relaxation at room temperature. However, our measurements for the $^3H_5$ lifetime at room temperature are 9.1 ± 0.5 ms, 8.6 ± 0.2 ms, and 9.5 ± 0.5 ms, for respective concentrations of 0.7, 1.5, and 3.0×10^{20} Tm^{3+} ions/cm^3. All our measurements are much longer than 5.51 ms and imply that had our crystals been cooled to 4.2 K, the lifetimes would be longer than those reported by Gandrud and Moos for 4.2 K.

Because of the discrepancy between our results and Gandrud and Moos we did not use their low-temperature lifetime measurement to determine the $^3H_5$ spontaneous emission rate A_2. To determine the spontaneous emission rate for the $^3H_5$ and the branching ratio β_{31} for the $^3H_4$, the rate model, Eqs. (13a)–(13d), was fit to the room-temperature emission data for these levels for the crystal with the lowest Tm^{3+} density, subject to the following constraints:

$$W_2 = A_2 + M_{21} \tag{25}$$

and

$$\frac{N_3}{N_2} = \frac{A_2\int_{1300\text{ nm}}^{1600\text{ nm}} \lambda I(\lambda)d\lambda}{\beta_{31}A_3\int_{1100\text{ nm}}^{1300\text{ nm}} \lambda I(\lambda)d\lambda} \tag{26}$$

and that all other parameters in the rate model be kept fixed on the results from previous analysis, Eqs. (17), (18), (20), and (22).

For Eq. (25), the inverse room-temperature lifetime for the $^3H_5$ level from Table I, 110 sec^{-1}, is used for W_2 since the $^3H_5$ room-temperature decay is exponential and cross-relaxation to the $^3H_5$, process C_2, is negligible for a low density sample [Eqs. (17) and (18)]. (The nonexponential $^3H_5$ decays occur at higher temperatures when C_2 becomes a significant process for populating the $^3H_5$.) Up-conversion is also assumed to be negligible and is therefore not included. Using the rate model to satisfy Eq. (26), required that $\beta_{31} = 0.14$ and $A_2 = 40$ sec^{-1}. Substitution of A_2 into Eq. (25) results in a room-temperature value for M_{21} of 70 sec^{-1}.

The spontaneous emission rate for the $^3H_5$ level, A_2, is much slower than expected from the results of Gandrud and Moos[11] but the room-temperature multiphonon rate is of the order expected from the energy-gap law, Eq. (3). The branch-

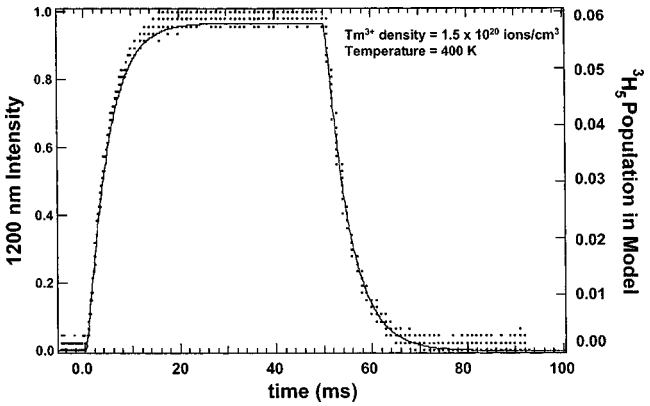

FIG. 12. Representative fit of the rate model fit to the transient rise and decay of 1200-nm fluorescence from the $^3H_5$ at 400 K for 1.5×10^{20} ions/cm^3 Tm^{3+} in YCl_3. Fit is with $U_3=0$, and $M_{21}=150\ \mathrm{sec}^{-1}$.

ing ratio values, $\beta_{31}=0.14$, $\beta_{32}=0$, and the remainder $\beta_{30}=0.86$, determined from the rate equation analysis are reasonable given that these same ratios for Tm^{3+} in $YLiF_4$ determined from Judd-Ofelt analysis are $\beta_{31}=0.095$, $\beta_{32}=0.0385$, and $\beta_{30}=0.866$.[2]

Comparison of rate model to data

From the preceding lifetime analysis, reasonable values of all parameters for the rate model, both spontaneous emission rates and temperature-dependent energy-transfer rates, are known, with the exception of M_{21} for temperatures greater than 300 K and any possible up-conversion rates. A fit of the entire model to the 1200-nm transients is used to determine the remaining unknown rates, before comparing the model's predictions to the temperature-dependent emission intensities.

Transient modeling

Fits were made using the entire rate model [Eqs. (13a)–(13d)] to the complete 1200-nm transients (including rise and fall) between 300 and 500 K for the three crystals at each 50-K temperature interval. Only U_3 (the up-conversion rate) and M_{21} (the $^3H_5$ multiphonon rate) were used as free parameters. The spontaneous emission rates and branching ratios determined by the previous analysis were kept temperature independent, while Eqs. (17), (18), (20), and (22), determined all the other temperature-dependent rates in the model. Branching from $^3H_5$ to $^3F_4$ is presumed small and β_{21} was set to zero. (A search for 4000-nm fluorescence corresponding to the $^3H_5$ to $^3F_4$ transition found none and β_{21} for other hosts is small, e.g., for Tm^{3+}:$YLiF_4$ $\beta_{21}=0.021$.[2]) Figure 12 is a representative transient showing 1200-nm fluorescence compared to the fit using the rate model. The transient shown in Fig. 12 is 1200-nm fluorescence from the crystal with 1.5×10^{20} ions/cm^3 at a temperature of 400 K. The fit required $M_{21}=150\ \mathrm{sec}^{-1}$ and $U_3=0$. Fits at all temperatures required $U_3=0$, a result consistent with our earlier assumption that the excited state densities

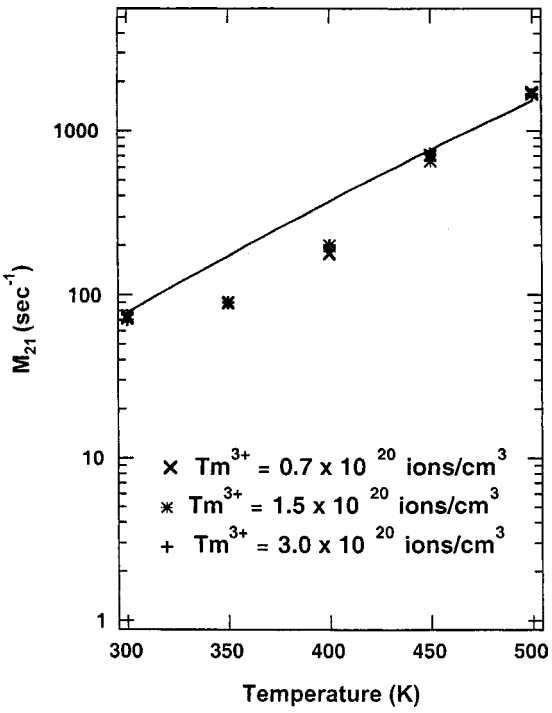

FIG. 13. Multiphonon relaxation rate of the $^3H_5$ level versus temperature (markers) compared to a fit for a mixed nine- and ten-phonon process (solid line).

resulting from the low excitation powers used (0.35 W), are insufficient to support up-conversion.

The $^3H_5$ multiphonon rates for all three crystals are plotted versus temperature in Fig. 13. As expected, the $^3H_5$ multiphonon rates are density independent, however, neither a purely nine-phonon nor ten-phonon process describes them. The complexity of $^3H_5$ multiphonon decay arises in part because only the lowest level of the Stark multiplet is able to decay by generating nine phonons. Relaxation from all other Stark levels must generate at least ten phonons. As the temperature rises, more ions populate the higher Stark levels shifting the temperature dependence to that of a ten-phonon process. Although the energy-gap law predicts slower multiphonon rates as the number of phonons increases, there are more ten-phonon generating levels (greater degeneracy), so the net zero-temperature rate from the ten-phonon processes is greater than for nine phonons.

A complete treatment of $^3H_5$ multiphonon relaxation requires use of Eq. (12), that determines the net multiphonon rate by averaging the rates from the individual Stark levels, weighted with an appropriate Boltzmann factor and degeneracy. However, a fit to Eq. (12) is difficult because of its many unknown parameters. For the purposes of developing a temperature-dependent rate model, it is more convenient to take a phenomenological approach. Assume that the $^3H_5$ multiphonon relaxation is from two levels separated by the energy of one phonon, $\hbar\omega=260\ \mathrm{cm}^{-1}$, each with degeneracy q_1 and q_2, respectively. The multiphonon rate can be approximated by

$$M_{21}=(1/Z)[q_1M_{21}^1(1+n)^9 + \exp(-\hbar\omega/kT)q_2M_{21}^2(1+n)^{10}], \qquad (27)$$

TABLE II. Rates for phonon-assisted energy transfer (temperature dependent). Zero-temperature ($T=0$), zero-density ($N=0$) rates obtained from fits to the theoretical temperature dependencies are listed.

Process	Number of phonons	Parameter	Zero-temperature rate	Uncertainty
Cross-relaxation: $^3H_4$–$^3F_4$	3	c_{m1}	8.4×10^{-19} ($cm^3\,sec^{-1}$)	$\pm1.0\times10^{-19}$ ($cm^3\,sec^{-1}$)
Cross-relaxation: $^3H_4$–$^3H_5$	−3	c_{m2}	8.4×10^{-19} ($cm^3\,sec^{-1}$)	$\pm1.0\times10^{-19}$ ($cm^3\,sec^{-1}$)
Multiphonon from $^3F_4$	20	M_{10}	2.5×10^{-3} (sec^{-1})	$\pm0.5\times10^{-3}$ (sec^{-1})
Multiphonon from $^3H_4$	15	M_{32}	0.15 (sec^{-1})	±0.05 (sec^{-1})
Multiphonon from (lower) $^3H_5$	9	M_{21}^1	3.5 (sec^{-1})	±0.9 (sec^{-1})
Multiphonon from (upper) $^3H_5$	10	M_{21}^2	2.6 (sec^{-1})	±0.6 (sec^{-1})

where $Z=[q_1+q_2\exp(-\hbar\omega/kT)]$ is the partition function for the two-level system and M_{21}^1 and M_{21}^2 are the respective zero-temperature multiphonon rates from the 1st and 2nd levels.

A fit to the data using Eq. (27) is shown in Fig. 13. There are six observed Stark levels for the $^3H_5$ state in YCl_3,[10] one level decays with nine phonons and five levels require greater than nine. For degeneracy values $q_1=1$ and $q_2=5$, the fit shown in Fig. 13 uses $M_{21}^1=3.5\,sec^{-1}$ and $M_{21}^2=2.6\,sec^{-1}$. The fit to Eq. (27) is poor, with the mid-temperature points appearing as unusually slow multiphonon rates compared to the temperature dependence given by Eq. (27). It is not possible to find a fit to Eq. (27) that includes both the high- and mid-temperature data. We chose to give greater weight to the high-temperature points since multiphonon relaxation becomes the more dominant rate as the temperature is raised. However, the fit chosen predicts a multiphonon rate of 370 sec^{-1} at 400 K, clearly faster than the 150-sec^{-1} rate for the 1200-nm transient shown in Fig. 12.

The longer than expected $^3H_5$ lifetimes are not the result of radiation trapping. The lifetimes are independent of sample density (see Table I) and occur in the sample with the lowest Tm^{3+} density where re-absorption of radiation into the $^3H_5$ is weak. Care was also taken during the lifetime measurements to pump small volumes near the sample surface. Again no dependence of lifetimes on the sample or the volume pumped occurred. It is not clear why Eq. (27) is inadequate for describing the temperature dependence of the $^3H_5$ relaxation rates.

Intensity modeling

Estimates for all non-negligible rate constants for Eqs. (13a)–(13d) are summarized in Tables II and III. The zero-temperature, zero density rates for the phonon-assisted processes, along with their uncertainties, are listed in Table II. The number phonons for each process, also in Table II, is substituted into Eq. (9) if the phonon number is positive or Eq. (10) if the phonon number is negative to determine the exact temperature dependence. The spontaneous emission rates are summarized in Table III along with their uncertainties and the wavelength of the transition and associated branching ratio.

The complete rate model, using rate constants in Tables II and III and their associated temperature dependencies, was run with a pump term $P(t)$ that matched the quasisteady-state conditions under which the fluorescence intensity data was obtained to predict the relative population of the first three excited-state levels. For comparison, relative populations of first three energy levels, $^3H_4$, $^3H_5$, and $^3F_4$, were deduced from the fluorescence intensity data, Fig. 5, by weighting with the appropriate wavelength, spontaneous emission rate and branching ratio, according to Eq. (24). Figures 14(a)–(c) compare the predicted quasisteady populations for all three crystals to those deduced from the data in Figs. 5(a)–(c) (solid lines are the rate model, markers represent data points). Figures 14(a)–(c), display excited-state populations as a function of temperature relative to the room-temperature population of the $^3F_4$ which for each crystal is normalized to 1. For a smooth prediction, Eq. (27) was used to represent the $^3H_5$ multiphonon rates, rather than the five discrete values shown in Fig. 13. Equations (17), (18), (20), and (22) were used for the other temperature-dependent energy-transfer rates. In generating the predictions shown in Figs. 14(a)–(c), only the Tm^{3+} density appropriate for the crystal and the temperature were varied in solving Eqs. (13a)–(13d).

The model accurately describes the temperature dependence of the $^3H_4$ and $^3F_4$ fluorescence intensities. The decrease in fluorescence as the temperature is raised results from the increase in multiphonon relaxation, Eqs. (20) and (22). The model predicts a shift downward relative to the $^3F_4$ in both the $^3H_4$ and $^3H_5$ emission as the Tm^{3+} density is increased because increased cross-relaxation shifts more population to the $^3F_4$. Figures 14(b) and (c) show that the fluorescence data has the predicted shift downward in $^3H_4$

TABLE III. Rates for radiative processes (temperature independent).

Transition	λ (nm)	Branching ratio	Rate (sec^{-1})	Uncertainty (sec^{-1})
$^3F_4$–$^3H_6$	1800	1	110	±10
$^3H_5$–$^3F_4$	4000	0 (<0.1)	0	<5
$^3H_5$–$^3H_6$	1200	1 (>0.9)	40	±5
$^3H_4$–$^3H_6$	800	0.86	600	±50
$^3H_4$–$^3F_4$	1490	0.14	100	±20
$^3H_4$–$^3H_5$	2400	0 (<0.05)	0	<40

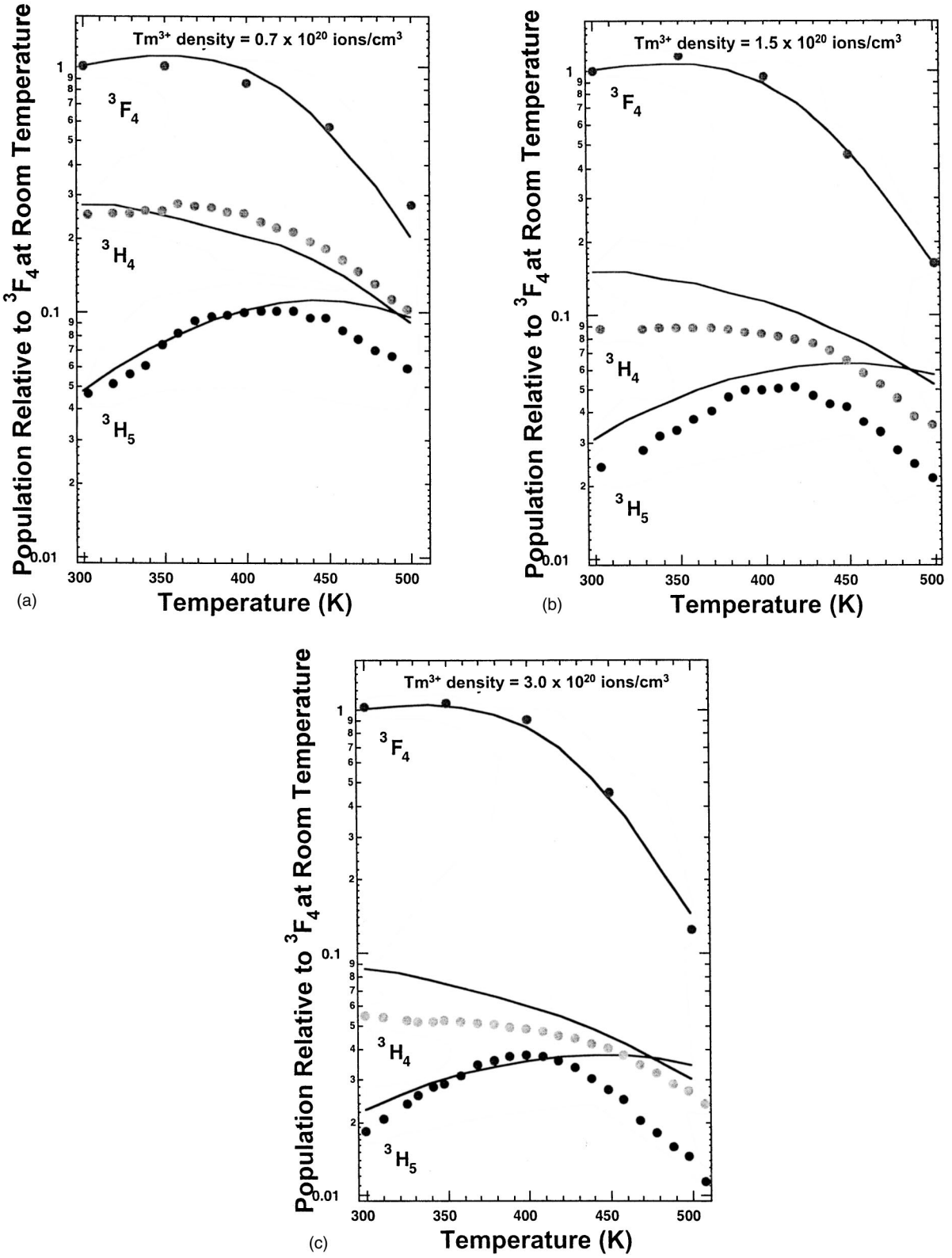

FIG. 14. Comparison of the rate model for the relative population of the three lower levels of Tm^{3+} (solid lines) to the measured relative populations (markers). The room-temperature $^3F_4$ population for each sample is normalized to 1. (a) 0.7×10^{20}, (b) 1.5×10^{20}, and (c) 3×10^{20} ions/cm^3 Tm^{3+} in YCl_3.

and $^3H_5$ emission, although the absolute level of emission intensity is not precisely predicted. The model predicts the observed increase in emission from the $^3H_5$ as the temperature rises from 300 to 400 K. The increase in $^3H_5$ emission results from the stronger temperature dependencies of the multiphonon (M_{32}) and cross-relaxation processes (C_2) feeding the level, compared to the weaker temperature dependence of the multiphonon process (M_{21}) draining it. However, above 400 K, multiphonon quenching dominates which prevents further increases in $^3H_5$ population. The model predicts a slower decrease with temperature in $^3H_5$ population above 400 K than observed.

CONCLUSION

Even in a reduced phonon energy host, phonon-assisted cross-relaxation remains an effective energy-transfer mechanism for diode-pumped Tm^{3+}. The reduced phonon energies enable radiation from the $^3H_5$, a level that does not radiate in traditional hosts, and allows for a detailed study of $^3H_5$ relaxation processes. Cross-relaxation of the $^3H_4$ level of Tm^{3+} in YCl_3 has both endothermic (to the $^3H_5$) and exothermic (to the $^3F_4$) channels. The exothermic rate is greater but the endothermic rate is more temperature dependent [Eq. (10)] and increases rapidly as the temperature is raised. However, rapid multiphonon quenching of all levels above 400 K prevents endothermic cross-relaxation from competing with exothermic cross-relaxation. Therefore no temperature exists where the endothermic and exothermic energy-transfer rates are in balance. To cool the crystal, a method for enhancing cross-relaxation to the $^3H_5$ needs to be found.

A rate model that uses the theoretical temperature dependencies for phonon-assisted processes shows that the most important parameter in describing the Tm^{3+} dynamics is the maximum lattice phonon energy $\hbar\omega$. The critical radius that results in cross-relaxation is about 15 Å, a distance typical for the electric-dipole-dipole interactions between Tm^{3+} ions in oxide and fluoride hosts.[4,5] The different behavior of Tm^{3+} in a chloride results primarily from the change in the host phonon energies, not a significant change in the electric-dipole-dipole interactions.

The model developed predicts most of the fluorescence intensities and fluorescence rise and decay features for the first three excited states of Tm^{3+}. The behavior of the $^3H_5$ level is not completely described by the model. The $^3H_5$ level is thinly populated, and achieves its population almost entirely by nonradiative energy transfer. The predicted $^3H_5$ population is especially sensitive to the rate model parameters and as a result it is an especially sensitive test of theories for the temperature dependence of energy transfer. It may be that approximations used in the theories are not completely valid for the $^3H_5$ level. If there are processes unaccounted for in the rate model that result in the longer than expected lifetimes for the $^3H_5$ level, those processes appear to be density independent since all three densities studied have the same behavior.

The rate model illustrates the effects that reduced phonon energies have in influencing Tm^{3+} energy transfer. It is expected that the model has general validity for predicting Tm^{3+} dynamics in other low phonon energy hosts.

ACKNOWLEDGMENTS

We thank Jessica DeAbreu for assistance in data analysis and preparing tables and figures. Work at Loyola College is supported by the National Science Foundation Division of Electrical and Communication Systems under Grant No. ECS 9970055. Work at the Naval Research Lab is supported by the Office of Naval Research.

*Fax: (410) 617-2646; electronic address: ganem@loyola.edu
†Fax: (202) 404-8695; electronic address: bowman@ccf.nrl.navy.mil

[1] L. B. Shaw, R. S. R. Chang, and N. Djeu, Phys. Rev. B **50**, 6609 (1994).
[2] Brian M. Walsh, Norman P. Barnes, and Baldassare Di Bartolo, J. Appl. Phys. **83**, 2772 (1998).
[3] Tso Yee Fan, G. Huber, Robert L. Byer, and P. Mitzscherlich, IEEE J. Quantum Electron. **24**, 924 (1988).
[4] Valentina A. French, Roger R. Petrin, Richard C. Powell, and Milan Kokta, Phys. Rev. B **46**, 8018 (1992).
[5] Stephen A. Payne, Larry K. Smith, Wayne L. Kway, John B. Tassano, and William F. Krupke, J. Phys.: Condens. Matter **4**, 8525 (1992).
[6] S. R. Bowman, M. J. Winings, R. C. Y. Auyeung, S. Searles, and B. J. Feldman, IEEE J. Quantum Electron. **27**, 2142 (1991).
[7] S. R. Bowman, G. J. Quarles, J. G. Lynn, and B. J. Feldman, *Optical Society of America Proceedings on Advanced Solid-State Lasers*, edited by Albert A. Pinto and T. Y. Fan (Optical Society of America, Washington, DC, 1993), Vol. 15, pp. 415–418.
[8] S. R. Bowman, J. E. Tucker, and Sean Kirkpatrick, *OSA Trends in Optics and Photonics*, Advanced Solid State Lasers Vol. 19, edited by Walter R. Bosenberg and M. Fejer (Optical Society of America, Washington, DC, 1998), pp. 519–523.
[9] C. Li, A. Lagriffoul, R. Moncorge, J. C. Souriau, C. Borel, and Ch. Wyon, J. Lumin. **62**, 157 (1994).
[10] G. H. Dieke, *Spectra and Energy Levels of Rare Earth Ions in Crystals*, edited by H. M. Crosswhite and H. Crosswhite (Interscience, New York, 1968).
[11] W. B. Gandrud and H. W. Moos, J. Chem. Phys. **49**, 2170 (1968).
[12] S. R. Bowman, B. J. Feldman, Joseph Ganem, and A. W. Kueny, IEEE J. Quantum Electron. **30**, 2925 (1994).
[13] S. R. Bowman, L. B. Shaw, B. J. Feldman, and Joseph Ganem, IEEE J. Quantum Electron. **32**, 646 (1996).
[14] Sean M. Kirkpatrick, L. B. Shaw, S. R. Bowman, S. Searles, B. J. Feldman, and Joseph Ganem, Opt. Express **1**, 78 (1997).
[15] S. R. Bowman, L. B. Shaw, S. Searles, B. J. Feldman, Sean, M. Kirkpatrick, Joseph Ganem, I. Gambaryan, T. Sanamyan, and E. Vartanyan, *OSA Trends in Optics and Photonics*, Advanced Solid State Lasers Vol. 19 (Ref. 8), pp. 534–537.
[16] M. C. Nostrand, R. H. Page, S. A. Payne, W. F. Krupke, P. G. Schunemann, and L. I. Isaenko, *OSA Trends in Optics and Photonics*, Advanced Solid State Lasers Vol. 19 (Ref. 8), pp. 524–528.

[17] M. C. Nostrand, R. H. Page, S. A. Payne, W. F. Krupke, P. G. Schunemann, and L. I. Isaenko, *OSA Trends in Optics and Photonics*, Advanced Solid State Lasers Vol. 26, edited by Martin M. Fejer, Hagop Injeyan, and Ursula Keller (Optical Society of America, Washington, DC, 1999), pp. 441–449.

[18] M. C. Nostrand, R. H. Page, S. A. Payne, P. G. Schunemann, and L. I. Isaenko, *OSA Trends in Optics and Photonics*, Advanced Solid State Lasers Vol. 34, edited by Hagop Injeyan, Ursula Keller, and Christopher Marshall (Optical Society of America, Washington, DC, 2000), pp. 446–453.

[19] Tkachuk, S. Ivanova, L. Isaenko, A. Yelisseyev, Steve Payne, R. Solarz, M. Nostrand, R. Page, and Stephen Payne, Acta Phys. Pol. A **95**, 381 (1999).

[20] Joseph Ganem, Paul Schmidt, and S. R. Bowman, presented at Optical Society of America Annual Meeting, Baltimore, MD 1998.

[21] S. R. Bowman, S. K. Searles, Joseph Ganem, and Paul Schmidt, *OSA Trends in Optics and Photonics*, Advanced Solid State Lasers Vol. 26 (Ref. 17), pp. 487–490.

[22] S. R. Bowman, S. K. Searles, N. W. Jenkins, S. B. Qadri, E. F. Skelton, and Joseph Ganem, *OSA Trends in Optics and Photonics*, Advanced Solid State Lasers Vol. 50, edited by Christopher Marshall (Optical Society of America, Washington, DC, 2001), pp. 154–156.

[23] L. Isaenko, A. Yelisseyev, A. Tkachuk, S. Ivanova, S. Vatnik, A. Merkulov, S. Payne, R. Page, and M. Nostrand, Mater. Sci. Eng., B **B81**, 188 (2001).

[24] M. C. Nostrand, R. H. Page, S. A. Payne, A. Yelisseyev, and L. I. Isaenko, J. Opt. Soc. Am. B **18**, 264 (2001).

[25] N. W. Jenkins, S. R. Bowman, L. B. Shaw, and J. R. Lindle, J. Lumin. **97**, 127 (2002).

[26] S. R. Bowman, IEEE J. Quantum Electron. **35**, 115 (1999).

[27] S. R. Bowman and Carl E. Mungan, *OSA Trends in Optics and Photonics*, Advanced Solid State Lasers Vol. 34 (Ref. 18), pp. 459–463.

[28] S. R. Bowman and C. E. Mungan, Appl. Phys. B: Lasers Opt. **B71**, 807 (2000).

[29] C. W. Hoyt, M. Sheik-Bahae, R. I. Epstein, B. C. Edwards, and J. E. Anderson, Phys. Rev. Lett. **85**, 3600 (2002).

[30] R. I. Epstein, M. I. Buchwald, B. C. Edwards, T. R. Gosnell, and C. E. Mungan, Nature (London) **377**, 500 (1995).

[31] P. Goldner and M. Mortier, J. Non-Cryst. Solids **284**, 249 (2001).

[32] A. Mendioroz, J. Fernanadez, M. Voda, M. Al-Saleh, R. Balda, and A. J. Garcia-Adeva, Opt. Lett. **27**, 1525 (2002).

[33] D. L. Dexter, J. Chem. Phys. **21**, 836 (1953).

[34] Toru Miyakawa and D. L. Dexter, Phys. Rev. B **1**, 2961 (1970).

[35] F. Auzel, Phys. Rev. B **13**, 2809 (1976).

[36] L. A. Riseberg and H. W. Moos, Phys. Rev. **174**, 429 (1968).

[37] A. I. Burshtein, Zh. Eksp. Teor. Fiz. **62**, 1695 (1972) [Sov. Phys. JETP **35**, 882 (1972)].

[38] T. Forster, Z. Naturforsch. B **49**, 321 (1949).

[39] A. A. Kaminskii, *Laser Crystals* (Springer-Verlag, Berlin, 1981).